INTERNATIONAL JOURNAL FOR NUMERICAL AND ANALYTICAL METHODS IN GEOMECHANICS
Int. J. Numer. Anal. Meth. Geomech., **23**, 141–160 (1999)

NUMERICAL MODELLING OF COUPLED FLOW AND DEFORMATION IN FRACTURED ROCK SPECIMENS

M. BAI[1]*, F. MENG[1], D. ELSWORTH[2], Y. ABOUSLEIMAN[3] AND J.-C. ROEGIERS[1]

[1] *Rock Mechanics Institute, Energy Ctr. P119, The University of Oklahoma, 100 E. Boyd St., Norman, OK 73019-1014, U.S.A.*
[2] *Department of Mineral Engineering, The Pennsylvania State University, University Park, PA 16802, U.S.A.*
[3] *Department of Civil Engineering, School of Engnieering and Architecture, The Lebanese American University, Byblos, Lebanon*

SUMMARY

A dual-porosity poroelastic model is extended to represent behaviour in cylindrical co-ordinates for the evaluation of flow-deformation effects in cylindrical laboratory samples incorporating a central wellbore or non-repeating axisymmetric injection on the periphery. Nine-node quadratic elements are used to represent mechanical deformation, while eight-node linear elements are used to interpolate the pressure fields, which offers significant advantages over the behaviour of other non-conforming elements. The model presented is validated against simplified analytical results, and extended to describe the behaviour of homogeneous and heterogeneous laboratory specimens subjected to controlled triaxial state of stress and injection tests. Apparent from the results is the significant influence of stress-deformation effects over system behaviour.

Key words: dual-porosity; poroelasticity; finite element; cylindrical co-ordinates

1. INTRODUCTION

Fluid flow through natural fractures has been a subject of interest for numerous years in the areas of energy exploitation and the development, protection and restoration of water resources. Due to the topological complexities associated with natural fractures, non-traditional approaches frequently have to be utilized to define fluid transmission and mass transport behaviour as a function of the distribution and behaviour of fractures within the porous matrix. Further, complications in quantifying flow are incurred when porous media are subject to additional loads such as stress and temperature variations. Coupled phenomena are difficult to represent, in part due to the poorly understood and complex response of natural media, but also due to the difficulty in adequately characterizing behaviour of the fracture component as subjected to variable stresses. Numerical methods may be used to unveil the vagaries of response to complex loads, accommodating varied degrees of coupling, as necessitated by the problem at hand.

Of critical importance is understanding the mechanisms by which anisotropic and heterogeneous permeability fields may develop[1,2] as a result of instantaneously applied mechanical loads,

*Correspondence to: M. Bai, Rock Mechanics Institute, Energy Ctr. P119, The University of Oklahoma, 100 E. Boyd St., Norman, OK 73019-1014, U.S.A.

Contract grant sponsor: National Science Foundation/State/Industry S/IUCRC program; contract grant number: EEC-9209619

CCC 0363–9061/99/020141–20$17.50 *Received 24 February 1997*
 Revised 9 March 1998

and transient diffusive pressure and thermal effects. These phenomena develop complex response that may only be represented by numerical means.

Extensive literature is available documenting the influence of deformation on fluid transmission, both in the field and in laboratory experiments. Bawden *et al.*[3] showed that increasing normal stress rapidly reduces permeability magnitudes, which may be associated with fracture compressibility. Louis[4] studied the influence of overburden stress variation on permeability measured at various depths in boreholes drilled in fractured formations. After examination of numerous test results, he concluded that the relationship between permeability and normal stress followed a negative exponential function. However, numerous fracture permeability tests show that this relationship does not often match real test data.[5]

The dominance of flow in fractures is exhibited in fractured crystalline rocks, such as granite, or in shales and clays where matrix blocks contribute negligible fluid mass to the highly conductive fractures. In contrast, fluid flow in unconsolidated materials such as gravels or highly permeable sandstones is essentially interstitial where flow routes may be rather tortuous. Fractured carbonate rocks such as limestones, clays or shales may comprise both permeable fractures and matrix blocks. Flow in such media may represent an intermediate characteristic between fracture flow and interstitial flow, approximating a dual-porosity response. In the dual-porosity poroelasticity system, the process of solid deformations coupled with the fluid flow is affected by the interaction between fractures and porous blocks. The behaviour of a dual porosity medium lacking coupling with the solid displacement field has been investigated since the early 1960s.[6–10] A special and restricted case of coupled dual-porosity poroelastic behaviour applicable to consolidation in fractured rock formations was presented by Duguid[11] and Duguid and Abel.[12] A generalized framework for flow through porous media with multiple porosity was introduced later and indepedently by Aifantis,[13,14] who employed a continum mixture formulation. The application of this theory has been completed either through analytical means,[15] or by numerical methods.[16]

Elsworth and Bai[17] presented an alternative dual-porosity poroelastic solution with application to two-dimensional geometry. Bai *et al.*[18] extended the traditional dual-porosity concept to the behaviour of generalized multiporous media with emphasis on reservoir ccharacteristics. The present study provides an improved dual-porosity poroelastic model developed in three-dimensional cylindrical co-ordinates, suitable for simulating coupled flow and deformation through fractured rock specimens prepared in the laboratory. This solution is further simplified for axisymmetric cases. In order to obtain precise coupling between displacement and pressure fields, quadratic displacement and linear pressure interpolation functions are chosen. A nine-node non-linear isoparametric brick element is used to achieve a higher-order interpolation for displacements than for pressures, in which an eight-node linear isoparametric brick element is used. This method achieves similar improvements as adding the non-conforming modes, but appears to be more robust than the latter approach. Attempts have been made to provide pressure as well as displacement contour profiles in a point injection/withdrawal situation. Parametric investigation focuses on identifying the influences of spatial heterogeneities on the pressure and deformation fields.

2. MODEL FORMULATION

Based on the coupled phenomena of fluid flow and solid deformation in a fractured porous medium, a set of coupled governing partial differential equations can be established with fluid

pressure and rock displacement as primary unknowns:[14,18]

$$G\frac{\partial^2 u_i}{\partial x_j \partial x_j} + (\lambda + G)\frac{\partial^2 u_j}{\partial x_i \partial x_j} + \alpha_1 \frac{\partial p_1}{\partial x_i} + \alpha_2 \frac{\partial p_2}{\partial x_i} = 0 \tag{1}$$

$$\frac{k_1}{\mu}\frac{\partial^2 p_1}{\partial x_i \partial x_i} + \alpha_1 \frac{\partial^2 u_i}{\partial t \partial x_i} - \beta_1 \frac{\partial p_1}{\partial t} - \omega(p_1 - p_2) = 0 \tag{2}$$

$$\frac{k_2}{\mu}\frac{\partial^2 p_2}{\partial x_i \partial x_i} + \alpha_2 \frac{\partial^2 u_i}{\partial t \partial x_i} - \beta_2 \frac{\partial p_2}{\partial t} + \omega(p_1 - p_2) = 0 \tag{3}$$

where subscripts 1 and 2, represent the matrix and fractures, respectively; λ and G are Lamé constants, α is the fluid pressure ratio factor or Biot coefficient,[19] β is the relative compressibility representing the lumped deformability of the fluid and the solid, k is the permeability, μ is the fluid dynamic viscosity, ω is the transfer coefficient, u is the solid displacement, and p is the fluid pressure.

2.1. Numerical formulation

The effective stress law for a dual-porosity medium may be expressed as:

$$\partial\boldsymbol{\sigma}_i = \partial\boldsymbol{\sigma}_i^{\mathrm{e}} + \mathbf{m}\alpha_i \partial p_i \tag{4}$$

where subscripts $i = 1$ and 2 represent the matrix and fractures, respectively, $\partial\boldsymbol{\sigma}$ are the total stresses, $\partial\boldsymbol{\sigma}^{\mathrm{e}}$ are the effective stresses, $\mathbf{m}$ is a one-dimensional binary vector and can be expressed as $\mathbf{m}^{\mathrm{T}} = (1\ 1\ 1\ 0\ 0\ 0)$ for a three-dimensional formulation.

Considering the linear relationship between stresses and strains, the modified effective stress law in a dual-porosity system may be expressed as[17]

$$\partial\boldsymbol{\sigma} = \mathbf{D}_{12}\left[\partial\boldsymbol{\varepsilon} + \sum_{i=1}^{2} \alpha_i \mathbf{C}_i \mathbf{m}\partial p_i\right] \tag{5}$$

where $\mathbf{D}_{12}$ is a composite elasticity matrix representing matrix and fractures and will be defined later, and $\mathbf{C}_i$ is the compliance matrix.

Substituting the modified effective stress law in equation (5) into the force equilibrium equation $\sigma_{ij,j} = 0$ where inertial effects are neglected, applying then the variational principle, and dividing through by Δt, the momentum balance in finite element form can be expressed as

$$\int_V \mathbf{B}^{\mathrm{T}}\mathbf{D}_{12}\mathbf{B}\,\mathrm{d}V\dot{\mathbf{u}} + \sum_{i=1}^{2}\alpha_i \int_V \mathbf{B}^{\mathrm{T}}\mathbf{D}_{12}\mathbf{C}_i\mathbf{m}\mathbf{M}\,\mathrm{d}V\dot{\mathbf{p}}_i = \int_S \mathbf{N}\,\mathrm{d}S\dot{\mathbf{f}} \tag{6}$$

where V is the volume of the integral domain, S is the domain surface on which traction $\mathbf{f}$ is applied, $\mathbf{M}$ and $\mathbf{N}$ are the vectors of shape functions interpolating fluid pressures and solid displacement, respectively, and $\mathbf{B}$ is the strain–displacement matrix, which will also be defined later.

Incorporating laminar flow and neglecting gravitational potential, Darcy's law can be written as

$$\mathbf{q}_i = \frac{-k_i}{\mu}\nabla p_i \tag{7}$$

where $\mathbf{q}_i$ is the vectors of fluid fluxes within matrix ($i = 1$) or fractures ($i = 2$).

Equating the devergence of Darcy's velocity in equation (7) to the rate of fluid accumulation due to all sources, such as the effect of temporal variation of volumetric strain, applying Galerkin's principle and pressure mapping functions, and neglecting the impact of fluid body force, the mass balance in finite element form may be given for each phase i as

$$\frac{1}{\mu}\int_V \mathbf{M}^{\mathrm{T}}\mathbf{k}_i\nabla\mathbf{M}\,\mathrm{d}V\mathbf{p}_i = \alpha_i\int_V \mathbf{N}^{\mathrm{T}}\mathbf{m}\mathbf{D}_{12}\mathbf{C}_i\mathbf{B}\,\mathrm{d}V\dot{\mathbf{u}} - \beta_i\int_V \mathbf{M}^{\mathrm{T}}\mathbf{M}\,\mathrm{d}V\dot{\mathbf{p}}_i \pm \omega\int_V \mathbf{M}^{\mathrm{T}}\mathbf{M}\,\mathrm{d}V\Delta\mathbf{p} + \int_V \mathbf{M}^{\mathrm{T}}\mathbf{M}\,\mathrm{d}V\mathbf{q}_i \tag{8}$$

where $\mathbf{q}$ is a vector of applied boundary fluid sources, and the sign $\pm$ is determined based on $i = 2$ and $i = 1$, respectively.

The matrix form of the finite element equations, for a representative time level after using a fully implicit finite difference scheme in the descretized time domain, may be established as

$$\frac{1}{\Delta t^{\phi}}\begin{bmatrix}\mathbf{A} & \mathbf{R}_1 & \mathbf{R}_2\\ \mathbf{R}_1^{\mathrm{T}} & \mathbf{G}_{11} & \mathbf{G}_{12}\\ \mathbf{R}_2^{\mathrm{T}} & \mathbf{G}_{21} & \mathbf{G}_{22}\end{bmatrix}\begin{bmatrix}\mathbf{u}\\ \mathbf{p}_1\\ \mathbf{p}_2\end{bmatrix}^{\phi} = \frac{1}{\Delta t^{\phi}}\begin{bmatrix}\mathbf{A} & \mathbf{R}_1 & \mathbf{R}_2\\ \mathbf{R}_1^{\mathrm{T}} & \mathbf{F}_1 & \mathbf{0}\\ \mathbf{R}_2^{\mathrm{T}} & \mathbf{0} & \mathbf{F}_2\end{bmatrix}\begin{Bmatrix}\mathbf{u}\\ \mathbf{p}_1\\ \mathbf{p}_2\end{Bmatrix}^{t} + \begin{bmatrix}\mathbf{f}\\ \mathbf{q}_1\\ \mathbf{q}_2\end{bmatrix}^{\phi} \tag{9}$$

where superscript T represents the matrix transposition, $\phi = t + \Delta t$, and

$$\mathbf{A} = \int_V \mathbf{B}^{\mathrm{T}}\mathbf{D}_{12}\mathbf{B}\,\mathrm{d}V \tag{10}$$

$$\mathbf{R}_1 = \alpha_1\int_V \mathbf{B}^{\mathrm{T}}\mathbf{D}_{12}\mathbf{C}_1\mathbf{m}\mathbf{M}\,\mathrm{d}V \tag{11}$$

$$\mathbf{R}_2 = \alpha_2\int_V \mathbf{B}^{\mathrm{T}}\mathbf{D}_{12}\mathbf{C}_2\mathbf{m}\mathbf{M}\,\mathrm{d}V \tag{12}$$

$$\mathbf{G}_{11} = -\frac{\Delta t^{\phi}}{\mu}\int_V \nabla\mathbf{M}^{\mathrm{T}}\mathbf{k}_1\nabla\mathbf{M}\,\mathrm{d}V - (\beta_1 + \Delta t\omega)\int_V \mathbf{M}^{\mathrm{T}}\mathbf{M}\,\mathrm{d}V \tag{13}$$

$$\mathbf{G}_{12} = \Delta t\omega\int_V \mathbf{M}^{\mathrm{T}}\mathbf{M}\,\mathrm{d}V, \quad \mathbf{G}_{21} = \mathbf{G}_{12}^{\mathrm{T}} \tag{14}$$

$$\mathbf{G}_{22} = -\frac{\Delta t^{\phi}}{\mu}\int_V \nabla\mathbf{M}^{\mathrm{T}}\mathbf{k}_2\nabla\mathbf{M}\,\mathrm{d}V - (\beta_2 + \Delta t\omega)\int_V \mathbf{M}^{\mathrm{T}}\mathbf{M}\,\mathrm{d}V \tag{15}$$

$$\mathbf{F}_1 = -\beta_1\int_V \mathbf{M}^{\mathrm{T}}\mathbf{M}\,\mathrm{d}V \tag{16}$$

$$\mathbf{F}_2 = -\beta_2\int_V \mathbf{M}^{\mathrm{T}}\mathbf{M}\,\mathrm{d}V \tag{17}$$

$$\mathbf{f} = \int_S \mathbf{N}\mathbf{f}^*\,\mathrm{d}S \tag{18}$$

$$\mathbf{q}_1 = \int_S \mathbf{M}\mathbf{q}_1^*\,\mathrm{d}S \tag{19}$$

$$\mathbf{q}_2 = \int_S \mathbf{M}\mathbf{q}_2^*\,\mathrm{d}S \tag{20}$$

where f^* is the surface traction, q^* is the fluid flux, **N** and **M** are the shape functions for a nine-node higher-order and an eight-node linear isoparametric elements, respectively.

In the finite element method, the shape functions are used to map the element displacements and fluid pressures at the nodal points. For the fluid pressure approximation in phase i, one has

$$\mathbf{p}_i^* = \mathbf{M}\mathbf{p}_i \tag{21}$$

or at the nodal level,

$$p_i^* = \sum_{j=1}^{8} M_j p_{ij}$$

where $\mathbf{p}_i$ is a vector of nodal pressure in phase i for the eight-node three-dimensional element. **M** is a vector of shape functions for pressure, which can be given in short form as

$$M_j = \tfrac{1}{8}(1 + \xi\xi_j)(1 + \eta\eta_j)(1 + \zeta\zeta_j) \tag{22}$$

where ξ, η, and ζ represent the local co-ordinates of the bi-unit cube with the origin at the centroid, and are confined by the magnitudes of -1 and 1, representing nodal co-ordinates ξ_j, η_j and ζ_j.

Although frequently used in practice,[20–24] it may be inappropriate to assume that the interpolation functions for solid displacements **N** and for fluid pressure **M** are identical. It is understood that the component of the partial stress tensor is continuously differentiable to the first order. As a result, the polynominal interpolation functions for the pore pressure distrubution must be one order lower than that chosen for the displacement field. Sandhu and Wilson[25] were among the first to apply the quadratic displacement and linear pressure expressions to evaluate finite element functions using triangular elements.

However, higher-order elements are frequently considered, creating computational difficulties being supposedly mathematically superior. To date, significant efforts have been devoted to determining the appropriate conditions for use, and advantage of using non-conforming shape functions (or incompatible mode).[26–31] By definition,[27] an incompatible mode is generated when the constant strain conditions are not satisfied for a four-node isoparametric quadrilateral element; or, in a more general sense, the shape functions are non-conforming if they are designed in such a manner that the continuity conditions for the displacement functions are different at different element interfaces. The focus of efforts is primarily is non-coupled elastic problems, such as beam bending analysis, in which the higher-order functions, similar to the analytical shear function in elastic beam theory,[32] are added to the linear displacement functions to improve computational accuracy. The results from these studies are incontrovertibly encouraging but are reflected in the development of suitable rectangular elements.[31] Taylor *et al.*[28] suggested a remedial approximation for arbitrarily shaped elements with an improvement in passing the patch test, however, only in limited and specific cases. According to our investigation, it appears that the suggested non-conforming shape functions are applicable only for certain bending problems to minimize the errors due to the difference between spurious shear and pure bending. However, the method may result in computational difficulties when used for other scenarios because the suggested non-conforming functions may improve the calculation for displacements only along certain element interfaces (e.g. vertical edges). This method may become especially suspect for higher dimensions (e.g. three-dimensional) even though the related functions were suggested by Wilson *et al.*[31] Furthermore, almost no data are available with the regard to the effect of the suggested method in the coupled poroelastic analysis, with one exception, by Khaled *et al.*,[16] who

applied the method in two-dimensions. However, no details were given in their study. In similar studies, our experience indicates increased difficulties in obtaining sensible results using the non-conforming shape functions, particularly for three-dimensional problems and when the element shape is non-rectangular. As a result, an alternative approach is investigated.

In this work, a quadratic displacement field and a linear pressure field are chosen. For the choice of a 3-D element, a higher-order representation can be accommodated by adding a central node to the element. This internal nodal variable is designed only to achieve a higher-order interpolation for the displacement than for the pressure. For the nine-node element (eight corner nodes and one central node), the expressions for the approximation in mapping nodal displacements may be described as

$$\mathbf{u}^* = \mathbf{N}\mathbf{u} \tag{23}$$

or at the nodal level,

$$u_r^* = \sum_{j=1}^{9} N_j u_{r_j}, \qquad u_\theta^* = \sum_{j=1}^{9} N_j u_{\theta_j}, \qquad u_z^* = \sum_{j=1}^{9} N_j u_{z_j}$$

where $\mathbf{u}$ is a vector of nodal displacements and $\mathbf{u}^{\mathrm{T}} = \{u_r, u_\theta, u_z\}$. $\mathbf{N}$ is a vector of shape functions for displacements. For the first eight nodes, $\mathbf{N}$ are chosen to be identical to $\mathbf{M}$ in equation (22). For the central node, however, $\mathbf{N}$ is given as follows:

$$N_9 = (1 - \xi^2)(1 - \eta^2)(1 - \zeta^2) \tag{24}$$

This higher-order shape function improves the elemental behaviour in the displacement and subsequent stress modes. For example, the present method does not possess any difficulties in passing the patch test, in comparison with other traditional non-conforming methods. Further comparative study is carried out to identify the importance of using the present method.[33] For a column consolidation using the three-dimensional elements, the present method with the linear pressure and non-linear displacement shape functions yields the accurate result, as indicated as the normalized values of mode 1 in Table I. In contrast, the method with the same order non-linear pressure and displacement shape functions leads to 2–5 percent deficiencies (see mode 2 in Table I), while the method using linear pressure and displacement shape functions results in 6–12 per cent surplus (see mode 3 of Table I), compared with the values in mode 1. Among the different modes, the one with the linear displacement shape function may produce the most inaccurate results.

For simplicity, the superscript * for variables in equations (21) and (23), indicating the finite element approximation, are omitted in the following description.

Table I. Comparative analysis of different shape functions

Mode	u_3	p_1	p_2	Note
1	1·00	1·00	1·00	Linear **p**, Nonlinear **u**
2	− 0·02	− 0·05	− 0·05	Nonlinear **p**, Nonlinear **u**
3	+ 0·12	+ 0·06	+ 0·06	Linear **p**, Linear **u**

Strains within a single element may be related to nodal displacements through the derivatives of the shape functions **B** as

$$\boldsymbol{\varepsilon} = \mathbf{B}\mathbf{u} \tag{25}$$

2.2. Matrices in cylindrical co-ordinates

The strain–displacement transformation matrix, **B**, is given by

$$\mathbf{B} = \begin{bmatrix} \dfrac{\partial}{\partial r} & 0 & 0 \\ 0 & \dfrac{\partial}{\partial z} & 0 \\ \dfrac{1}{r} & 0 & \dfrac{1}{r}\dfrac{\partial}{\partial \theta} \\ \dfrac{\partial}{\partial z} & \dfrac{\partial}{\partial r} & 0 \\ \dfrac{1}{r}\dfrac{\partial}{\partial \theta} & 0 & \dfrac{\partial}{\partial r} - \dfrac{1}{r} \\ 0 & \dfrac{1}{r}\dfrac{\partial}{\partial \theta} & \dfrac{\partial}{\partial z} \end{bmatrix} \mathbf{N} \tag{26}$$

$\mathbf{D}_{12}$ is the elasticity matrix, which is the inverse of the composite compliance matrix **C**, as

$$\mathbf{D}_{12} = (\mathbf{C}_1 + \mathbf{C}_2)^{-1} = \frac{1}{|\mathbf{D}_{12}|} \begin{bmatrix} d_{11} & \mathrm{d}_{12} & \mathrm{d}_{13} & 0 & 0 & 0 \\ d_{21} & \mathrm{d}_{22} & \mathrm{d}_{23} & 0 & 0 & 0 \\ d_{31} & \mathrm{d}_{32} & \mathrm{d}_{33} & 0 & 0 & 0 \\ 0 & 0 & 0 & d_{44} & 0 & 0 \\ 0 & 0 & 0 & 0 & d_{55} & 0 \\ 0 & 0 & 0 & 0 & 0 & d_{66} \end{bmatrix} \tag{27}$$

where the individual components are

$$|\mathbf{D}_{12}| = \left[\frac{1}{K_{sh}s} + \frac{2(1+v)}{E}\right]^3 \left[\left(\frac{1}{E} + \frac{1}{K_n s}\right)^3 - \frac{3v^2}{E^2}\left(\frac{1}{K_n s} + \frac{1}{E}\right) - \frac{2v^3}{E^3}\right] \tag{28}$$

$$d_{11} = d_{22} = d_{33} = \left[\frac{1}{K_{sh}s} + \frac{2(1+v)}{E}\right]^3 \left[\left(\frac{1}{E} + \frac{1}{K_n s}\right)^2 - \frac{v^2}{E^2}\right] \tag{29}$$

$$d_{12} = d_{21} = d_{13} = d_{31} = d_{23} = d_{32} = \left[\frac{1}{K_{sh}s} + \frac{2(1+v)}{E}\right]^3 \left[\frac{v}{E}\left(\frac{1}{E} + \frac{1}{K_n s}\right) + \frac{v^2}{E^2}\right] \tag{30}$$

$$d_{44} = d_{55} = d_{66} = \left[\frac{1}{sK_{sh}} + \frac{2(1+v)}{E}\right]^2 \left[\left(\frac{1}{K_n s} + \frac{1}{E}\right)^3 - \frac{3v^2}{E^2}\left(\frac{1}{E} + \frac{1}{K_n s}\right) - \frac{2v^3}{E^3}\right] \tag{31}$$

and E is the elastic modulus, v is Poisson's ratio, s is the homogeneous fracture spacing, K_n is the fracture normal stiffness, and K_{sh} is the fracture shear stiffness.

$\mathbf{k}_1$ and $\mathbf{k}_2$ are the permeability tensors for matrix and fracture as follows:

$$\mathbf{k}_i = \begin{bmatrix} (k_{rr})_i & (k_{r\theta})_i & (k_{rz})_i \\ (k_{\theta r})_i & (k_{\theta\theta})_i & (k_{\theta z})_i \\ (k_{zr})_i & (k_{z\theta})_i & (k_{zz})_i \end{bmatrix}, \quad i = 1, 2 \tag{32}$$

The integration region is a three-dimensional cylindrical domain. As an example, at the element level, the stiffness matrix $\mathbf{A}$ can be written as

$$\mathbf{A} = \int_{-1}^{1}\int_{-1}^{1}\int_{-1}^{1} \mathbf{B}^{\mathrm{T}}\mathbf{D}\mathbf{B}|\mathbf{J}|r\,\mathrm{d}\xi\,\mathrm{d}\eta\,\mathrm{d}\zeta \tag{33}$$

where $|\mathbf{J}|$ is a Jacobian determinant, ξ, η and ζ represent local co-ordinates, r is the radius of the cylindrical domain, which can be approximated as

$$r = \bar{r} = \frac{\sum_{i=1}^{j} r_i}{j} \tag{34}$$

where j is the number of nodes per element.

2.3. Matrices in axisymmetric co-ordinates

For the case that the domain is axisymmetric with respect to the z-axis while the loads and material properties are axisymmetric, the three-dimensional cylindrical problem may be degenerated to a two-dimensional system. In view of the present problem, the displacements u and v occur in the r and z directions in a cylindrical co-ordinate system, where the displacement w in the θ direction remains unchanged since the changes of stress and pressure are independent of angular co-ordinate θ. Consequently, shearing strains $\gamma_{r\theta}$ and $\gamma_{z\theta}$ also vanish. The strain–displacement transformation matrix, $\mathbf{B}$, reduces to

$$\mathbf{B} = \begin{bmatrix} \dfrac{\partial}{\partial r} & 0 \\ 0 & \dfrac{\partial}{\partial z} \\ \dfrac{1}{r} & 0 \\ \dfrac{\partial}{\partial z} & \dfrac{\partial}{\partial r} \end{bmatrix} \mathbf{N} \tag{35}$$

The elasticity matrix $\mathbf{D}_{12}$ and the related compliance matrix $\mathbf{C}_i$ can be expressed as

$$\mathbf{D}_{12} = (\mathbf{C}_1 + \mathbf{C}_2)^{-1} = \frac{1}{|\mathbf{D}_{12}|} \begin{bmatrix} d_{11} & d_{12} & d_{13} & 0 \\ d_{21} & d_{22} & d_{23} & 0 \\ d_{31} & d_{32} & d_{33} & 0 \\ 0 & 0 & 0 & d_{44} \end{bmatrix} \tag{36}$$

where

$$|\mathbf{D}_{12}| = \left[\frac{1}{K_{sh}s} + \frac{2(1+v)}{E}\right]\left[\left(\frac{1}{E} + \frac{1}{K_n s}\right)^3 - \frac{3v^2}{E^2}\left(\frac{1}{K_n s} + \frac{1}{E}\right) - \frac{2v^3}{E^3}\right] \tag{37}$$

$$d_{11} = d_{22} = d_{33} = \left[\frac{1}{K_{sh}s} + \frac{2(1+v)}{E}\right]\left[\left(\frac{1}{E} + \frac{1}{K_n s}\right)^2 - \frac{v^2}{E^2}\right] \tag{38}$$

$$d_{12} = d_{21} = d_{13} = d_{31} = d_{23} = d_{32} = \left[\frac{1}{K_{sh}s} + \frac{2(1+v)}{E}\right]\left[\frac{v}{E}\left(\frac{1}{E} + \frac{1}{K_n s}\right) + \frac{v^2}{E^2}\right] \tag{39}$$

$$d_{44} = \left[\frac{1}{sK_{sh}} + \frac{2(1+v)}{E}\right]^2\left[\left(\frac{1}{K_n s} + \frac{1}{E}\right)^3 - \frac{3v^2}{E^2}\left(\frac{1}{E} + \frac{1}{K_n s}\right) - \frac{2v^3}{E^3}\right] \tag{40}$$

The integration region is in a two-dimensional axisymmetric domain. Again, at the element level, the stiffness matrix **A** can be written as

$$\mathbf{A} = 2\pi\int_{-1}^{1}\int_{-1}^{1}\mathbf{B}^{\mathrm{T}}\mathbf{D}\mathbf{B}|\mathbf{J}|r\,\mathrm{d}\xi\,\mathrm{d}\eta \tag{41}$$

where r can be determined from equation (34).

3. MODEL VERIFICATION

The numerical models presented in cylindrical and axisymmetric co-ordinates are verified against some existing solutions, as described in the following.

3.1. Case 1

For a thick hollow cylinder with flow across the domain, the present numerical solution is compared with the analytical solution.[34] The finite element mesh layout and boundary conditions in cylindrical co-ordinates are depicted in Figure 1, where only a quarter of the domain is shown due to symmetry. There are total 64 elements and 125 nodes. Permeability anisotropy in the radial and vertical orientations is considered. The data used in the calculation are listed in Table II (Column (a)). Because the verification is against single-porosity behaviour, flow through fractures is maintained at a minimum by assigning vanishing porosity and negligible permeability.

Figure 2 shows the comparison of pore pressure between numerical and analytical solutions subject to various ratios of radial to vertical permeabilities. It is assumed that k_r is equal to k_θ in the horizontal plane. Agreement between numerical and analytical results is excellent. It is apparent that increased radial permeability results in the earlier pressure variation, indicating the more dominant flow along that orientation.

3.2. Case 2

The second case tests both cylindrical and axisymmetric models. The simulation is related to radial flow through a confined homogeneous aquifer where the analytical solution is available from Mueller and Witherspoon.[35]

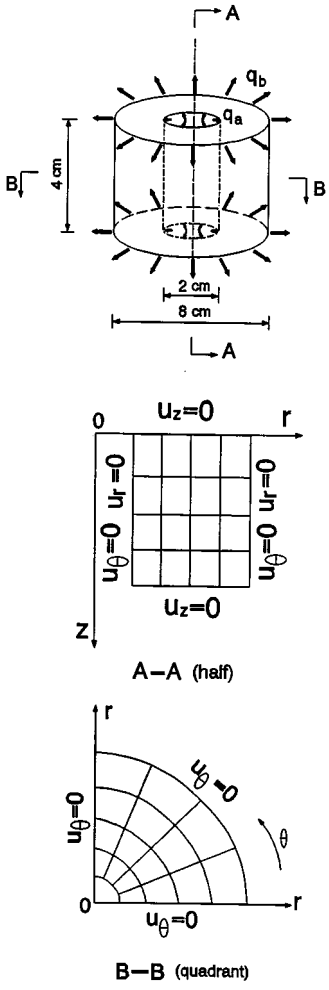

Figure 1. Mesh layout of flow in a hollow cylinder

Table II. Selected parameters for verification and modelling

Parameter	Unit	(a)	(b)	(c)	(d)	(e)
Elastic modulus E	MN/m_2	100	10	1	10	1
Poisson's ratio v	—	0·2	0·2	0·2	0·25	0·25
Internal flow rate q_a	m_3/s	0·8	0·5	1	5	5
External flow rate q_b	m_3/s	0·4	—	0	4	4
Fracture stiffness K_n	$MN/m^2/m$	2	20	0·1	1·1	0·1
Fluid bulk modulus K_f	MN/m^2	0·1	0·01	0·001	0·01	0·01
Matrix porosity n_1	—	0·3	0·2	0·4	0·4	0·4
Fracture porosity n_2	—	0·0	0·0	0·1	0·1	0·1
Matrix permeability k_1/μ	$m^4/(MN\,s)$	10^{-8}	10^{-10}	10^{-5}	10^{-5}	10^{-6}
Fracture permeability k_2/μ	$m^4/(MN\,s)$	10^{-25}	10^{-25}	0·1	0·1	0·01
Fracture spacing s	m	1	1·25	0·2	1·2	0·2

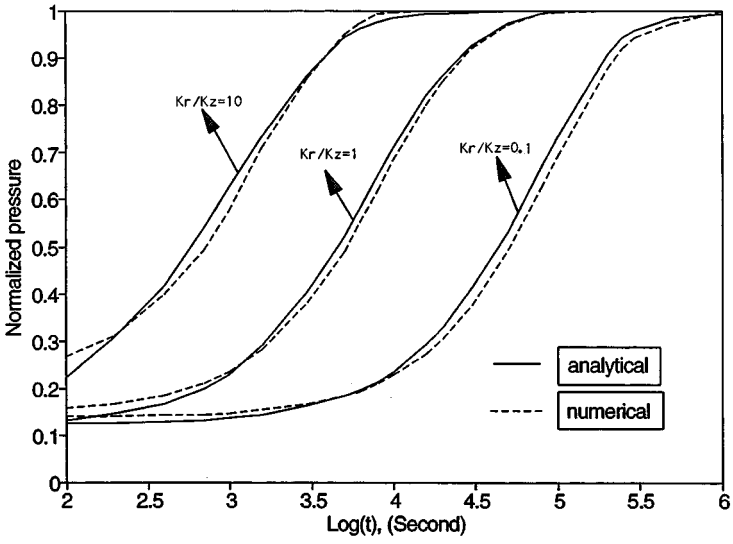

Figure 2. Comparison of temporal pore pressures

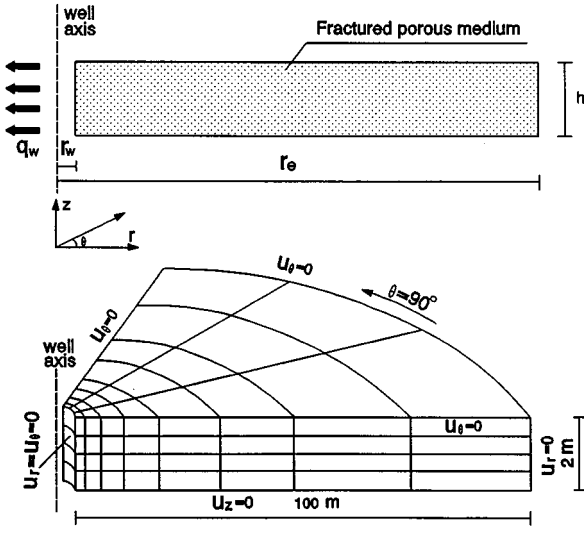

Figure 3. Mesh layout of flow in a cylindrical domain

A production situation is considered with a well of radius r_w and constant flow rate q_w. The well penetrates an aquifer with outer radius r_e and thickness h. Figure 3 shows the schematic mesh layout and boundary conditions. In the analysis, 32 elements and 45 nodes are used for the axisymmetric model, while 96 elements and 180 nodes are used for the cylindrical model. A variable mesh spacing along the radial direction has been adopted to enhance the numerical

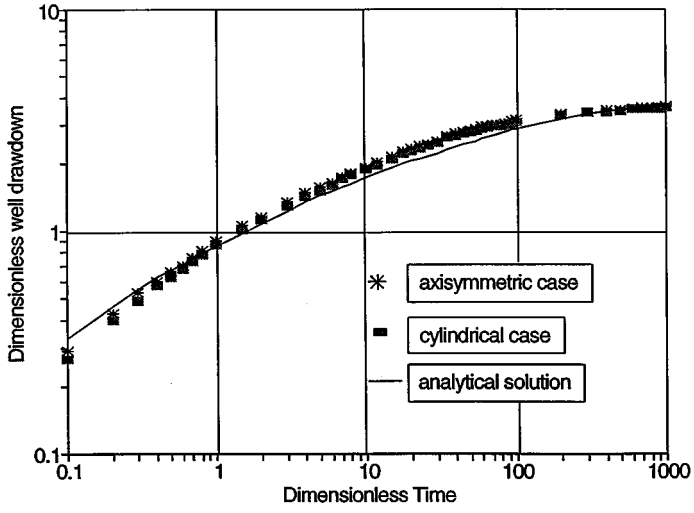

Figure 4. Comparison of well drawdowns

accuracy. Parameters used in the simulation are given in Table II (Column (b)). Again, the equivalent single-porosity conceptualization is used for comparison purposes.

Figure 4 illustrates the comparison of well drawdown between the presented axisymmetric and cylindrical models and analytical solution. Again, an excellent match is obtained. It should be pointed out that Valliappan and Khalili–Naghadesh[20] examined this case using an alternative dual-porosity poroelastic formulation. They were also able to match the analytical solution.

4. NUMERICAL SIMULATION OF LABORATORY TESTING

It is common practice to determine the permeability of rock specimens though either transient or steady state injection and withdrawal techniques in which either pore pressure or flow rate is measured in the laboratory environment. Incorporating the effect of loading and induced stresses on the pore pressure, response is less common. Under such conditions, numerical investigation of such effects appears to be of prime interest, as demonstrated in the following, where only the transient fluid loading is considered.

Field injection or pumping through a centrally located well can be simulated by either divergent or convergent flow tests via a central hole in the laboratory rock sample. Figure 5 shows a cylindrical sample with a point injection inside the central hole and the configuration of the finite element meshes. Because both geometry and loading are symmetric to the vertical axis, the axisymmetric finite element model can be used to predict variations of stress and pore pressure. The nine basic parameters for the calculation, as introduced in the previous formulation, are listed in Table II (Column (c)). Figure 6 shows the normalized pressure, radial and vertical stresses as a result of fluid injection.

In the laboratory determination of permeability of rock sample, a point injection is usually made through the side of the sample, such as shown in Figure 7 where the determination of

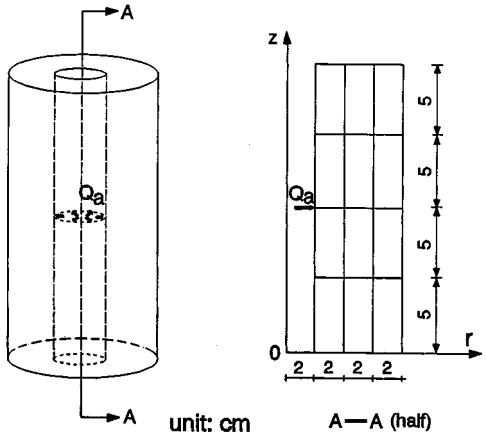

Figure 5. Mesh layout of an axisymmetric model

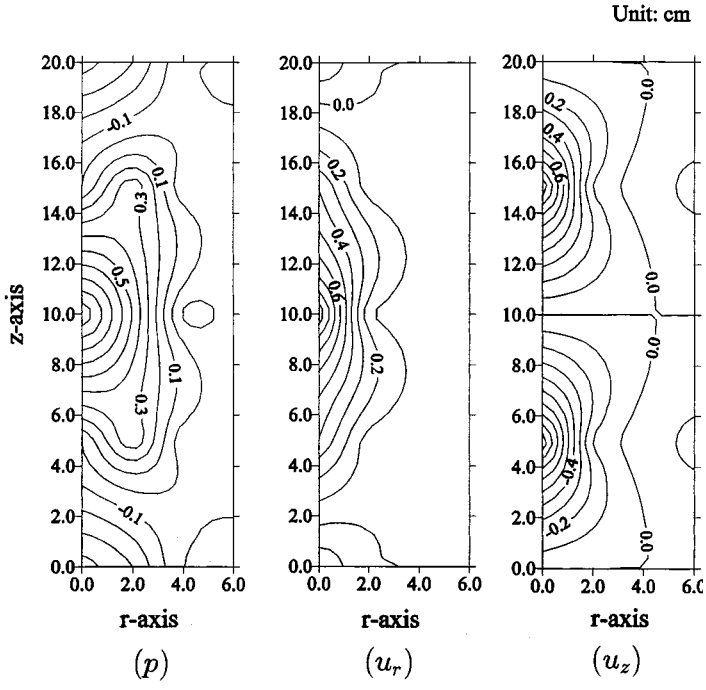

Figure 6. Spatial distribution of pressure and displacements

horizontal permeability is desired. Under such circumstances, the axisymmetric model cannot be used because the loading configuration is not symmetric to the vertical axis. Ideally, the cylindrical model described in this paper can be used for the simulation. For the convenience of mesh layout, a 3-D finite element model in Cartesian coordinate is chosen for the simulation.[36]

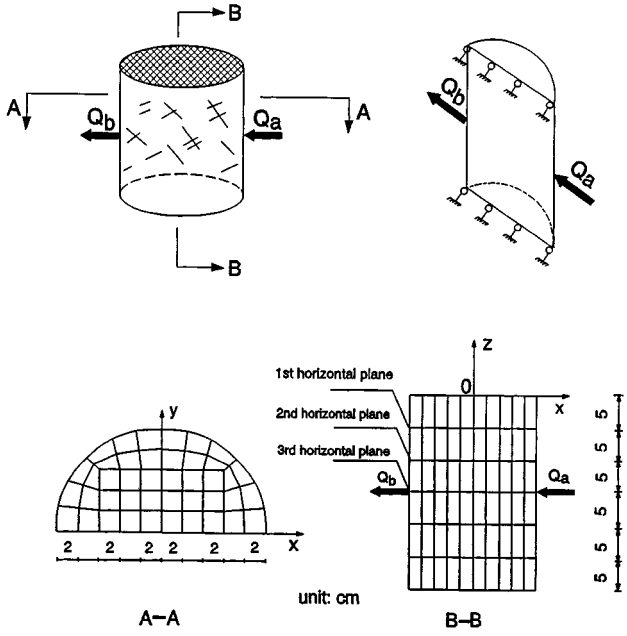

Figure 7. Mesh layout of a point injection and withdrawal

The finite element arrangement is depicted also in Figure 7, where total number of nodes and elements are 378 and 252, respectively. The parameters used in calculation are given in Table II (column(d)).

Figure 8 illustrates the normalized displacements along horizontal and vertical directions, together with the normalized fluid pressure 5000 seconds after the initiation of loading. Radical changes of horizontal displacement are obvious near the inlet and the outlet, where the negative values imply that the displacement is opposite to the x-axis direction. The peak changes of vertical displacement can be located at the upper and lower portions approximately one third distance between the inlet/outlet and top/bottom surfaces of the sample, due to the sample constraints. The pressure profile is similar to that of horizontal displacement.

The changes of the normalized displacement and pressure in three different horizontal planes (marked in Figure 7) are further examined. Figures 9, 10 and 11 describe the distribution of the normalized displacements along x-, y- and z-axis directions along with the normalized pressure profiles within the three different horizontal planes 5000 seconds after the initiation of loading, respectively. It should be noted that u_z vanishes at the third plane due to the symmetry. In comparison, the displacement and pressure are most uniformly distributed in the plane farthest from the source/sink (e.g. the first plane). This indicative influences of stresses on pressure at different places has been verified through examining the case with a pure elastic deformation. Pore pressures are displayed relative to a pre-withdrawal ambient fluid pressure of zero, hence negative pore pressures are negative relative to this benchmark.

The influence of formation heterogeneities can be identified by spatially varying modeling parameters. In this analysis, the heterogeneities of the formation are studied by placing two

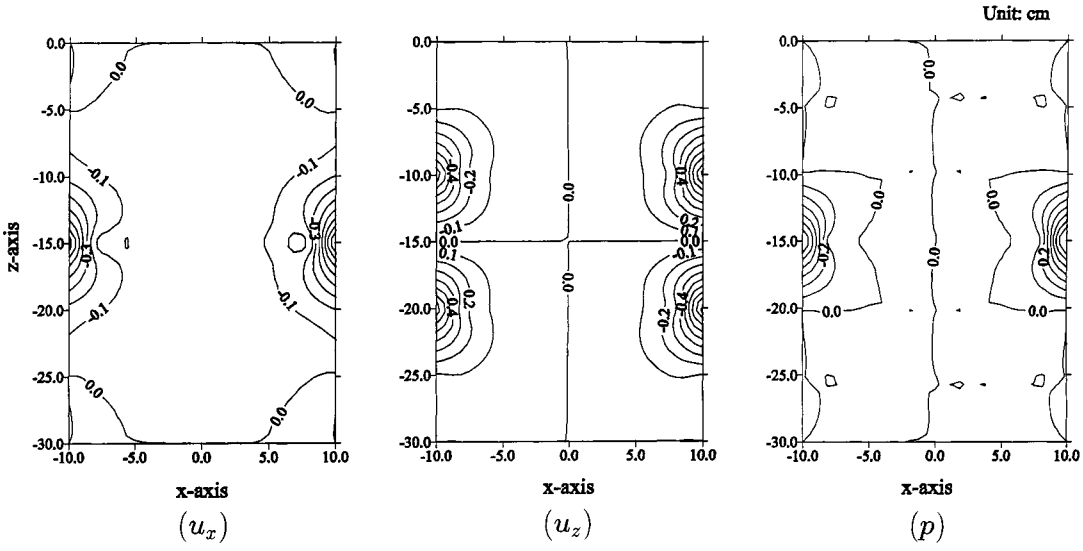

Figure 8. Spatial distribution of pressure and displacements

different kinds of materials in the domain, as shown in Figure 12. The modelling parameters in the dark area of Figure 12 are given in Table II (column(e)), as the opposite of the other areas listed in Table II (column(d)). The softer material (lower elasticity modulus), smaller fracture stiffness and fracture spacings are typical parameters chosen for the latter case, replicating the inhomogeneous soft bands in the otherwise homogeneous media.

Figure 13, 14 and 15 describe the normalized displacements along the x, y and z-axis directions and the normalized pressure profiles at three different horizontal planes as shown in Figure 7. Indeed the displacement and pressure contours show the largest differences in magnitudes between homogeneous (Figure 9) and heterogeneous (Figure 13) rocks at the first plane, due to the existence of the soft layer between planes 1 and 2. The results in the other planes show less radical differences between the homogeneous and heterogeneous media.

5. CONCLUSIONS

A dual-porosity poroelastic finite element formulation in cylindrical co-ordinate is presented to study the interactive behaviour of fluid flow and rock deformation for stress controlled injection tests in a fractured rock specimen. The numerical formulation for the simplified axisymmetric configuration is also given for the study with specific loading conditions and material properties. Accurate coupling between the quadratic displacement and linear pressure fields is preserved to achieve an improved numerical approximation in comparison with the traditional non-conforming formulation. Numerical solutions are verified against some simplified analytical results with excellent agreement. Numerical analysis attempts to replicate laboratory experiments where both divergent flow through a centrally-located borehole and point injection and collection across a cylindrical rock specimen are incorporated. The results reveal the significant influences of stress variations on the changes in fluid pressure during the transient period of fluid flow. Rock

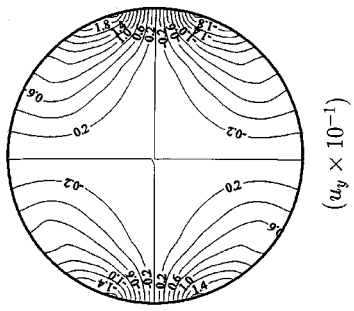

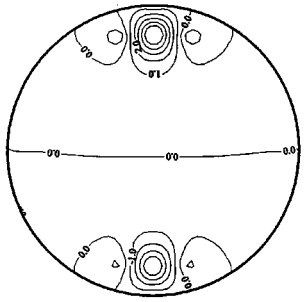

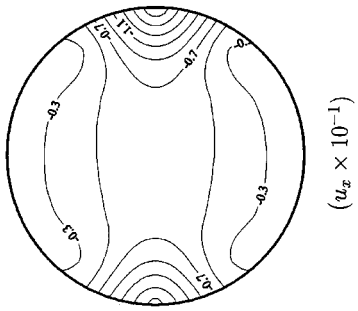

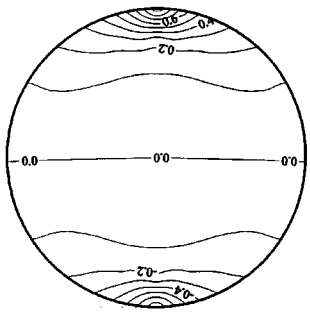

Figure 10. Distribution of pressure and displacements in second plane

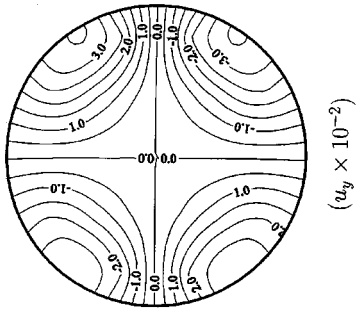

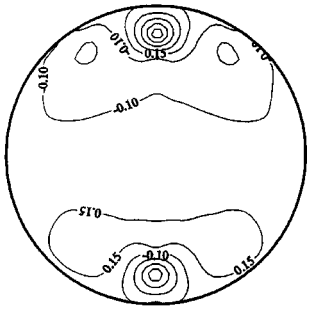

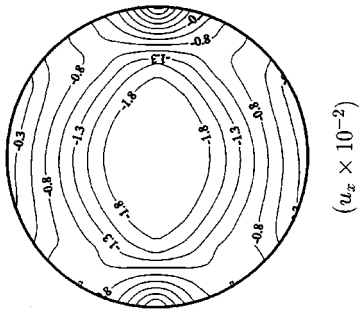

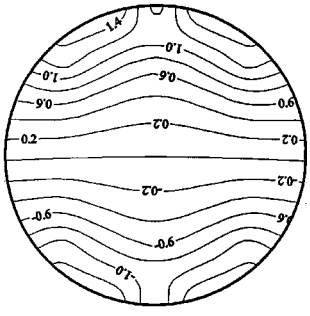

Figure 9. Distribution of pressure and displacements in first plane

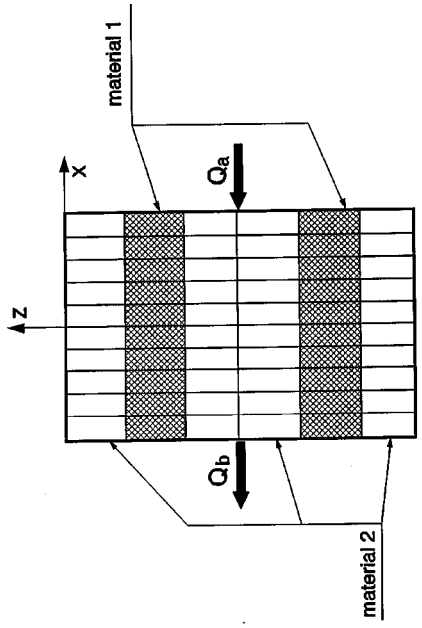

Figure 12. A heterogeneous rock sample

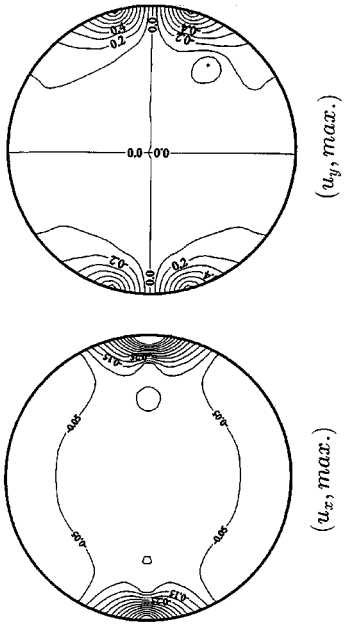

Figure 11. Distribution of pressure and displacements in third plane

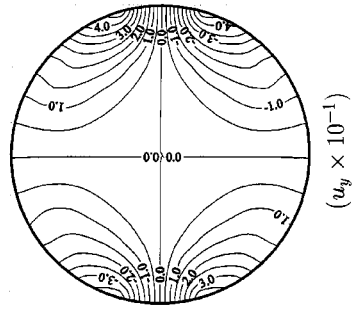

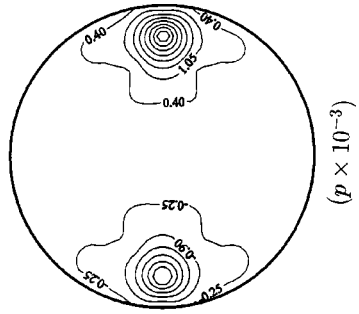

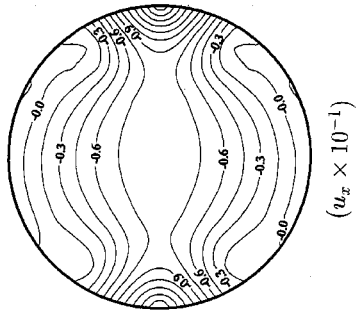

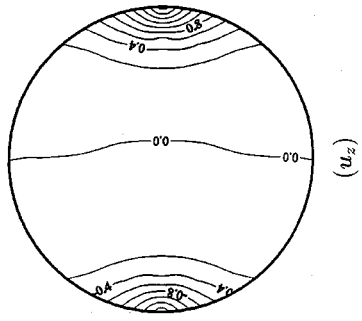

Figure 14. Distribution of pressure and displacements in second plane

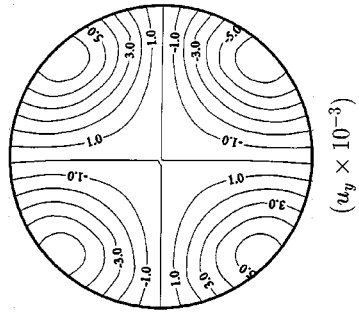

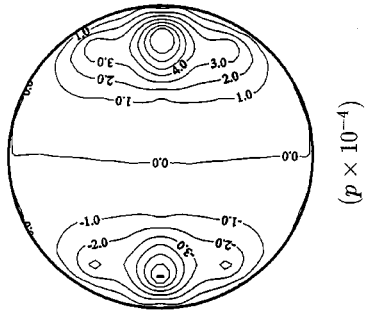

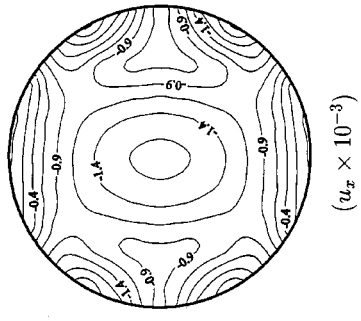

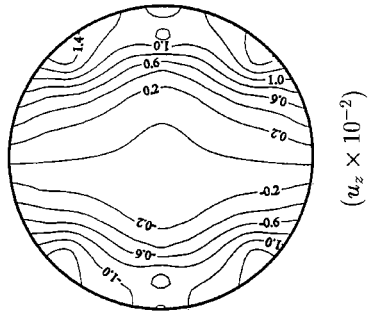

Figure 13. Distribution of pressure and displacements in first plane

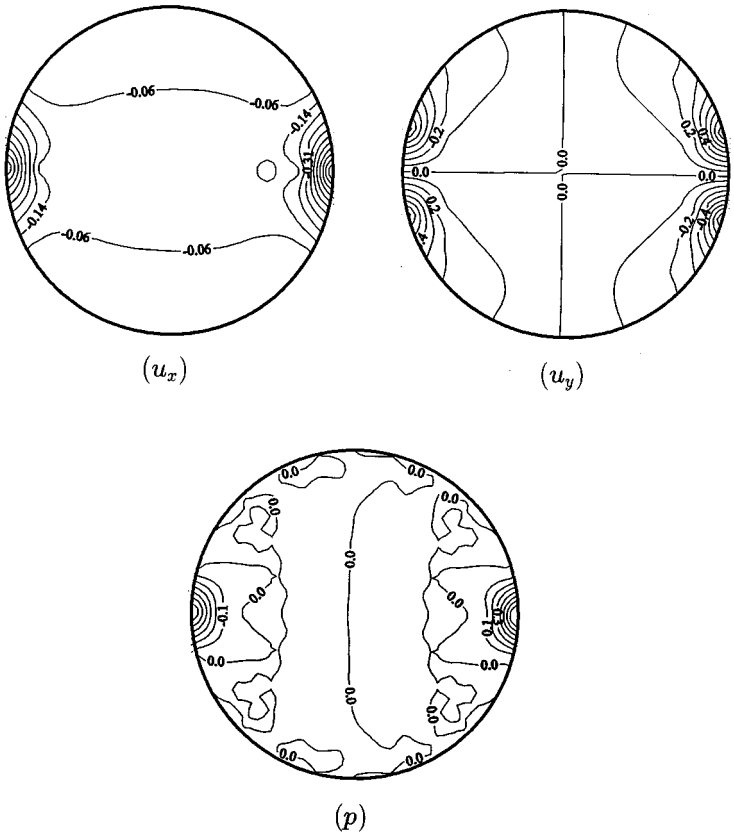

Figure 15. Distribution of pressure and displacements in third plane

heterogeneities may play an important role to channel the fluid flow, where soft rock materials may form natural barriers to isolate the poroelastic impact in a localized area.

ACKNOWLEDGEMENT

Support of the National Science Foundation/State/Industry under the S/IUCRC program and under the contract EEC-9209619, the constructive comments and suggestions from Drs. M. Zaman and M. Kanj, along with help in the graphical presentation from Mr. J. Cao, are gratefully acknowledged.

REFERENCES

1. R. A. Greenkorn, 'Directional permeability of heterogeneous anisotropic porous media', *Soc. Petroleum Engng. J.*, **16,** 124–132 (1964).
2. W. F. Brace, 'Permeability from resistivity and pore shape', *J. Geophys. Res.*, **82,** 3343–3349 (1977).
3. W. F. Bawden, J. H. Curran and J.-C. Roegiers, 'Influence of fracture deformation on secondary permeability—a numerical approach', *Int. J. Rock Mech. Min. Sci. Geomech. Abstr.*, **17,** 265–79 (1980).

4. C. Louis, 'Rock hydraulics', in *Rock Mechanics*, Springer, Vienna, 1974, pp. 299–382.
5. P. A. Witherspoon, Y. W. Tsang, J. C. S. Long and J. Noorishad, 'New approaches to problems of fluid flow in fractured rock masses', *Proc. 22nd U.S. Symp. Rock Mech.*, MIT Press, Cambridge, MA, 1982.
6. G. I. Barenblatt, I. P. Zheltov and N. Kochina, 'Basic concepts in the theory of seepage of homogeneous liquids in fissured rocks', *Prikl. Mat. Mekh.*, **24,** 852–864 (1960).
7. J. E. Warren and P. J. Root, 'The Behavior of naturally fractured reservoirs', *J. Soc. Pet. Engng.*, **3,** 245–255 (1963).
8. N. S. Boulton, 'Analysis of data from non-equilibrium pumping tests allowing for delayed yield from storage', *Proc. Inst. Civ. Engng.*, **26,** 469–482 (1963).
9. P. J. Closmann, 'An aquifer model for fissured reservoirs', *Soc. Pet. J.*, **15,** 385–398 (1975).
10. P. S. Huyakorn, B. H. Lester and J. W. Mercer, 'An efficient finite element technique for modeling transport in fractured porous media, 1. Single-species transport', *Water Resour. Res.*, **19,** 841–854 (1983).
11. J. Duguid, 'Flow in fractured porous media', *Ph.D. Thesis*, Princeton University, Princeton, NJ, 1973.
12. J. Duguid and J. Abel, 'Finite element Galerkin method for flow in fractured media', in *Finite Element Methods in Flow Problems*, University of Alabama Press, University, Alabama, 1974.
13. E. C. Aifantis, 'Introducing a multi-porous medium', *Dev. Mech.*, **9,** 209–211 (1977).
14. E. C. Aifantis, 'On the problem of diffusion in solids', *Acta Mechanica*, **37,** 265–296 (1980).
15. R. K. Wilson and E. C. Aifantis, 'On the theory of consolidation with double porosity', *Int. J. Engng. Sci.*, **20,** 1009–1035 (1982).
16. M. Y. Khaled, D. E. Beskos and E. C. Aifantis, 'On the theory of consolidation with double porosity', *Int. J. Numer. Anal. Meth. Geomech.*, **8,** 101–123 (1984).
17. D. Elsworth and M. Bai, 'Flow-deformation response of dual-porosity media', *J. Geotech. Engng. ASCE*, **118,** 107–124 (1992).
18. M. Bai, D. Elsworth and J.-C. Roegiers, 'Multi-porosity/multi-permeability approach to the simulation of naturally fractured reservoirs', *Water Resour. Res.*, **29,** 1621–1633 (1993).
19. M. A. Biot, 'General theory of three dimensional consolidation', *J. Appl. Phys.*, **12,** 155–164 (1941).
20. S. Valliappan, and N. Khalili-Naghadeh, 'Flow through fissured porous media with deformable matrix', *Int. J. Numer. Meth. Engng.*, **29,** 1079–1094 (1990).
21. N. Khalili-Naghadeh and S. Valliappan, 'Flow through fissured porous media with deformable matrix: implicit formulation', *Water Resour. Res.*, **27,** 1703–1709 (1991).
22. H.-D. Yeh, R.-H. Lu and G.-T. Yeh, 'Finite element modeling for land displacements due to pumping', *Int. J. Numer. Anal. Meth. Geomech.*, **20,** 79–99 (1996).
23. H. R. Ghafouri and R. W. Lewis, 'A finite element double porosity model for heterogeneous deformable porous media', *Int. J. Numer. Anal. Meth. Geomech.*, **20,** 831–844 (1996).
24. P. S. Huyakorn, B. H. Lester and C. R. Faust, 'Finite element techniques for modeling groundwater flow in fractured aquifers', *Water Resour. Res.*, **19,** 1019–1035 (1983).
25. R. S. Sandhu, and E. L. Wilson, 'Finite element analysis of seepage in elastic media', *J. Engng. Mech. ASCE*, **95,** 641–652 (1969).
26. M. J. Turner, R. W. Clough, H. C. Martin and L. J. Topp, 'Stiffness and deflection analysis of complex structures', *J. Aeronaut. Sci.*, **23,** 805–854 (1956).
27. O. C. Zienkiewicz, '*The Finite Element Method*', 3rd edn, McGraw-Hill, London, 1977.
28. R. L. Taylor, P. J. Beresford and E. L. Wilson, 'A non-conforming element for stress analysis', *Int. J. Numer. Meth. Engng.*, **10,** 1211–1219 (1976).
29. M. Froier, L. Nilsson and A. Samuelsson, 'The rectangular plane stress element by Turner, Pian and Wilson', *Int. J. Numer. Meth. Engng.*, **8,** 433–437 (1974).
30. E. L. Wilson, 'The static condensation algorithm', *Int J. Numer. Meth. Engng.*, **8,** 198–203 (1974).
31. E. L. Wilson, R. L. Taylor, W. P. Doherty and J. Ghaboussi, 'Incompatible displacement models', in *Numerical and Computer Methods in Structural Mechanics*, Academic Press, New York, 1973, pp. 43–57.
32. S. Timoshenko and J. N. Goodier, *Theory of Elasticity*, 2nd edn, McGraw-Hill, New York, 1951.
33. M. Bai, 'A comparative analysis between higher order and nonconforming elements', unpublished study.
34. J. Cao, M. Bai and M. Zaman, 'Study of radial fluid flow in anisotropic media: analytical approach', *Report RMC-96-07*, 1996.
35. T. D. Mueller and P. A. Witherspoon, 'Pressure interface effects within reservoirs and aquifers', *Trans. AIME*, **234,** 471–474 (1965).
36. M. Bai, D. Elsworth, J.-C. Roegiers and F. Meng, 'A three-dimensional dual-porosity poroelastic model', *Proc. CCMRI—Int. Mining Tech'95*, Beijing, China, 1995, pp. 184–202.

